Capillary hydrodynamic fractionation of hydrophobic colloids: Errors in the estimated particle size distribution

Luis A. Clementi [a,b], Zohartze Artetxe [c], Ziortza Aguirreurreta [c], Amaia Agirre [c], José R. Leiza [c], Luis M. Gugliotta [a], Jorge R. Vega [a,b,*]

[a] INTEC (CONICET and Universidad Nacional del Litoral), Güemes 3450 (3000), Santa Fe, Argentina
[b] FRSF-UTN (Facultad Regional Santa Fe-Universidad Tecnológica Nacional), Lavaisse 610 (3000), Santa Fe, Argentina
[c] POLYMAT, Kimika Aplikatua Saila, Kimika Zientzien Fakultatea, University of the Basque Country UPV/EHU, Joxe Mari Korta Zentroa, Tolosa Hiribidea 72, 20018 Donostia-San Sebastián, Spain

ABSTRACT

Capillary hydrodynamic fractionation (CHDF) with turbidity detection at a single wavelength is an analytical technique that is often used for sizing the sub-micrometric particles of hydrophobic colloids. This article investigates three sources of errors that affect the particle size distribution (PSD) estimated by CHDF: diameter calibration errors, uncertainties in the particle refractive index (PRI), and instrumental broadening (IB). The study is based on simulated and experimental examples that involve unimodal and bimodal PSDs. Small errors in the diameter calibration curve can produce important deviations in the number average diameter due to systematic shifts suffered by the PSD modes. Moderate uncertainties in the PRI are unimportant in the analysis of unimodal PSDs, but in the specific case of bimodal PSDs, errors in the PRI can strongly affect the estimated number concentration of each mode. The typical IB correction (based on the IB function estimated from narrow standards) produces slightly erroneous average diameters but can lead to PSDs with underestimated widths and distorted shapes. In practice, the three investigated sources of errors can be present simultaneously, and uncertainties in the average diameters, the shape and width of the PSD, and the number concentration of the PSD modes are unavoidable.

© 2014 Published by Elsevier B.V. on behalf of Chinese Society of Particuology and Institute of Process Engineering, Chinese Academy of Sciences.

Introduction

Polymeric colloids (or latexes) are obtained by emulsion, miniemulsion, microemulsion, and dispersion polymerization and are typically used in paints, inks, coatings, adhesives, etc. The particle size distribution (PSD) of a latex can strongly affect the rheological, mechanical, and physical properties of the final product. An accurate knowledge of the PSD is necessary not only for characterizing the latex but also for understanding the physicochemical mechanisms that occur in the course of polymerization (Gugliotta, Clementi, & Vega, 2010).

Capillary hydrodynamic fractionation (CHDF) is a simple and relatively fast technique that is often used for estimating the PSD of colloidal systems (DosRamos & Silebi, 1990; Silebi & DosRamos, 1989). In CHDF, the particles are first separated according to their size in a capillary tube. Then, a turbidity detector (at a single wavelength) is used to estimate the number of particles in each eluted fraction. Currently, Matec Applied Science (USA) is the only worldwide supplier of commercial CHDF equipment.

In CHDF, the particles transported by the carrier fluid exhibit a typical parabolic velocity profile (i.e., maximum at the capillary center and null at the capillary walls). The center of a spherical particle of diameter D immersed in the carrier fluid is excluded from a layer of thickness $D/2$ adjacent to the capillary wall (the exclusion layer). As a consequence of the pseudo-random movement across the capillary, the particles can experience only the carrier velocities over a reduced cross-sectional area far enough from the capillary wall. Thus, smaller particles are affected by a thin exclusion layer and experience lower average velocities. In contrast, larger particles are affected by a wide exclusion layer and are dragged by the

* Corresponding author at: INTEC (CONICET and Universidad Nacional del Litoral), Güemes 3450 (3000), Santa Fe, Argentina. Tel.: +54 0342 4511595; fax: +54 0342 4511079.
E-mail addresses: jvega@santafe-conicet.gov.ar, jorgerubenvega@gmail.com (J.R. Vega).

high velocity stream of the capillary center. In summary, larger particles are transported at higher average axial velocities than smaller particles, and a fractionation according to particle sizes is obtained (DosRamos & Silebi, 1990; Silebi & DosRamos, 1989).

The CHDF measurement procedure consists of the following sequential steps: (i) the injection of a diluted sample of the particle dispersion; (ii) the injection of a marker solution (approximately 60–120 s after the sample injection); (iii) the measurement of a UV signal at a single wavelength (λ_0); (iv) the numerical filtering of the noisy UV signal to improve its signal-to-noise ratio; and (v) the calculation (at discrete times, t_i) of the baseline-corrected fractogram, $\tau(t_i)$. The marker is a small molecular species (e.g., sodium dichromate) that elutes at a high time, t_m. This value is used to calculate the relative rate of transport of the particles through the capillary and to correct for undesired flow variations.

The ordinates of the discrete number PSD, $f(D_i)$, represent the number fraction of particles contained in the diameter interval $[D_i, D_i + \Delta D]$ ($i = 1, \ldots, N$), where ΔD is a regular partition of the D axis. In principle, all particles of size D_i elute at a common time, t_i, and the relative elution time, R_i, is defined as (DosRamos & Silebi, 1990):

$$R_i = \frac{t_m}{t_i}. \tag{1}$$

Then, the R_i-based fractogram, $\tau_R(R_i)$, is obtained from $\tau(t_i)$, as follows:

$$\tau_R(R_i) = \tau(t_i) \frac{1}{\left| dR_i/dt_i \right|} = \tau(t_i) \frac{1}{t_m/t_i^2}, \tag{2}$$

where the factor (t_m/t_i^2) corrects the ordinates of $\tau(t_i)$ due to the non-linear transformation of Eq. (1). Then, $f(D_i)$ is calculated as follows (Bohren & Huffman, 1983; DosRamos & Silebi, 1990):

$$f(D_i) = \frac{k_f \tau_R(R_i)}{Q_{ext}[\lambda_0, n_m(\lambda_0), n_p(\lambda_0), D_i(R_i)] D_i^2(R_i)} \frac{1}{dD_i(R_i)/dR_i}, \tag{3a}$$

where the particle extinction efficiency, $Q_{ext}[\lambda_0, n_m(\lambda_0), n_p(\lambda_0), D_i(R_i)]$, is calculated through the Mie scattering theory (Bohren & Huffman, 1983) and represents the light extinction (at λ_0) caused by a spherical particle of diameter D_i and particle refractive index (PRI) $n_P(\lambda_0)$, with the particle immersed in a medium of refractive index $n_m(\lambda_0)$; $D_i(R_i)$ is the calibration curve that assigns a relative elution time R_i at a given diameter D_i; and $dD_i(R_i)/dR_i$ is used to correct the ordinates of $\tau_R(R_i)$ for the non-linear transformation involved in the first factor of the right-hand side of Eq. (3a). The normalization factor k_f was included to ensure $\sum f(D_i) = 1$. Note that the calculation of Q_{ext} requires knowledge of $n_P(\lambda_0)$, which is only available for a small number of materials. Some methods for estimating the real and imaginary components of $n_P(\lambda_0)$ of colloidal dispersions are available (see, e.g., Lechner, Colfen, Mittal, Volkel, & Wohlleben, 2011). In practice, however, the PRI of polystyrene (PS) is often used when $n_P(\lambda_0)$ is unknown, and this approach can lead to meaningful errors in the estimated PSD.

As an alternative to a number-based PSD, a volume-based PSD can also be derived. In fact, a discrete volume PSD, $v(D_i)$, represents the volume fraction of particles contained in $[D_i, D_i + \Delta D]$. Bearing in mind that $v(D_i) \propto f(D_i) D_i^3$, then Eq. (3a) can be rewritten as:

$$v(D_i) = \frac{k_v \tau_R(R_i)}{Q_{ext}[\lambda_0, n_m(\lambda_0), n_p(\lambda_0), D_i(R_i)]/D_i(R_i)} \frac{1}{dD_i(R_i)/dR_i}, \tag{3b}$$

where the factor k_v ensures $\sum v(D_i) = 1$. As a consequence of the implicit nonlinear transformation given by $v(D_i) \propto f(D_i) D_i^3$, the shapes of $f(D_i)$ and $v(D_i)$ are significantly different when the size distribution is broad or multimodal (e.g., a small number fraction

of large particles can produce a large volume fraction because large particles are more strongly weighted by D_i^3 in the volume PSD).

Eqs. (3a) and (3b) indicate that the raw measurement in a CHDF experiment with single turbidity detection cannot be considered as intrinsically representative of a number- or volume-based PSD. In fact, in both cases, the raw measurement must be corrected not only by the Mie extinction effect ($Q_{ext} D_i^2$ or Q_{ext}/D_i) but also by the slope of the calibration curve (dD_i/dR_i). The importance of a proper Mie correction for estimating accurate PSDs has been reported in the measurement of latexes through analytical ultracentrifugation with turbidity detection (Lechner et al., 2011). For simplicity, in what follows, only number PSDs will be considered.

The usual procedure for obtaining the calibration curve $D_i(R_i)$ involves the injection of J narrow standards of known diameters $\bar{D}_j$ ($j = 1, \ldots, J$), and their relative elution times $R_j = t_m/t_j$ are arbitrarily assigned at the peaks of the fractograms. The calibration curve $D_i(R_i)$ is obtained by fitting the pairs $\{\bar{D}_j, R_j\}$ with a known function, typically a polynomial or a sigmoid function, as follows:

$$D_i(R_i) = k_n R_i^n + k_{n-1} R_i^{n-1} + \cdots + k_0, \quad \text{(polynomial calibration)} \tag{4}$$

$$D_i(R_i) = K_3 - \frac{1}{K_2} \ln\left(\frac{K_1}{R_i} - 1\right). \quad \text{(sigmoid calibration)} \tag{5}$$

The main advantages of the CHDF technique are as follows: (i) a PSD can be obtained in a few minutes after injection (e.g., 20 min); (ii) high efficiency for identifying multiple modes; and (iii) simple operation, even for poorly trained users. However, CHDF also exhibits important drawbacks: (i) it is a relative technique (i.e., a diameter calibration is required); (ii) the PRI must be approximately known; and (iii) the width and/or shape of the estimated PSD can be erroneous due to an inaccurate instrumental broadening (IB) correction.

The IB is an important cause of imperfect resolution in CHDF and can strongly affect the estimation of narrow PSDs or multimodal distributions with narrow modes. The IB is a consequence of the finite injection volume and detection cell volume, the non-uniform parabolic velocity profile in the capillary, and the Brownian motion of the particles, which affects their axial displacements (DosRamos & Silebi, 1990). Due to IB, a single species of diameter D_i will exhibit a range of elution times instead of a single t_i. As a consequence, the measured fractogram $\tau^m(t_i)$ is wider than the ideal IB-free fractogram $\tau(t_i)$, thus producing an estimated PSD with an overestimated width. The discrete and linear mathematical model that relates $\tau(t_i)$ and $\tau^m(t_i)$ is given by DosRamos and Silebi (1990), as follows:

$$\tau^m(t_i) = \sum_{i^*=1}^{N^*} g(t_i, t_{i^*}) \tau(t_{i^*}), \tag{6}$$

where t_{i^*} ($i^* = 1, \ldots, N^*$) is the discrete elution time corresponding to the ideal IB-free fractogram, and $g(t_i, t_{i^*})$ is the normalized IB function (IBF), i.e., $\sum_{i^*=1}^{N^*} g(t_i, t_{i^*}) = 1$.

Eq. (6) can be used to correct the IB provided that $g(t_i, t_{i^*})$ is known. In the more general case, the IB correction includes the following steps: (i) estimating $g(t_i, t_{i^*})$; (ii) inverting Eq. (6) to obtain the corrected (IB-free) fractogram, $\tau^c(t_i)$, from $\tau^m(t_i)$ and $g(t_i, t_{i^*})$; and (iii) obtaining the estimated PSD, $f^c(D_i)$, from $\tau^c(t_i)$ and Eqs. (2) and (3a). The key step (i) normally assumes that a set of J monodisperse standards of known diameters $\bar{D}_j$ ($j = 1, \ldots, J$) is available. Then, $g(t_i, t_{i^*})$ is obtained by interpolation of the J fractograms $\tau_j^m(t_i)$.

Unfortunately, strictly monodisperse standards are currently not commercially available, and only a crude estimation of $g(t_i,t_{i^*})$ is possible.

The numerical inversion of Eq. (6) can be implemented through different methods (Gugliotta, Vega, & Meira, 1990). The iterative method proposed by Ishige, Lee, and Hamielec (1971) is often used, and the corrected fractogram in the rth iteration is calculated through:

$$\tau_r^c(t_i) = \frac{\tau^m(t_i)}{\sum_{i^*=1}^{N^*} g(t_i, t_{i^*}) \tau_{r-1}^c(t_{i^*})} \tau_{r-1}^c(t_i), \quad (r = 1,2,3,\ldots) \tag{7}$$

with $\tau_0^c(t_i) = \tau^m(t_i)$. Convergence of Eq. (7) is reached when its denominator tends to the measured fractogram $\tau^m(t_i)$. As a consequence of the unavoidable measurement noise, highly oscillating solutions are typically obtained at high values of r. For this reason, the iterative procedure is normally truncated after a few iterations. Note that a wrong kernel $g(t_i,t_{i^*})$ will distort the shape of the estimated fractogram.

Several authors have utilized CHDF to size colloidal systems. For example, DosRamos and Silebi (1990) utilized CHDF to estimate multimodal PSDs of PS latex. In their work, the estimated average diameters were different from those obtained by transmission electron microscopy (TEM), but the shapes of the PSDs were acceptably recovered. Miller, Venkatesan, Silebi, Sudol, and El-Aasser (1994) and Erdem, Sully, Sudol, Dimonie, and El-Aasser (2000) successfully used CHDF to monitor the size and stability of submicrometer oil droplets in miniemulsions. Miller, Sudol, Silebi, and El-Aasser (1995) used CHDF to monitor the PSD of a PS latex during miniemulsion polymerization, and their results were in good agreement with estimations obtained by TEM. Jung and Shul (2003) employed CHDF to estimate the PSD of zeolites during crystallization reactions. The estimated PSDs were acceptable when compared with those obtained by TEM and scanning electron microscopy (SEM). Chu, Graillat, Guillot, and Guyot (1997) and Elizalde, Leal, and Leiza (2000) compared different techniques to measure the PSD of unimodal and multimodal latex samples. The former showed that sedimentation of the samples followed by dynamic light scattering (DLS) of the multimodal latexes provided PSDs comparable with other fractionation techniques (e.g., field flow fractionation and CHDF). However, the authors observed that the results depended on the polymer system and the particle size. Elizalde et al. (2000) blended submicrometric PS standards to produce bimodal and trimodal samples, and the performances of CHDF, DLS, and a disk centrifuge photosedimentometer (DCP) were assessed in terms of the determination of the two or three modes present, the accuracy of the average diameter of the peaks, and the number concentration of each mode, compared with the known amounts used in their preparation. The authors concluded that CHDF was the best technique for multimodal samples, followed by DCP and DLS. In their study, only samples of known PRI were analyzed. More recently Mariz, De La Cal, and Leiza (2010, 2011) used CHDF to measure the evolution of PSD during the seeded semi-batch emulsion polymerization of methyl methacrylate, butyl acrylate, and acrylic acid (MMA/BA/AA). The goal was to produce latexes of high solids content with low viscosity. To achieve this goal, an innovative polymerization strategy was proposed that required the production of a bimodal latex with a well-defined particle size and number concentration of each mode. Finally, Mariz (2011) found that the PSD obtained by CHDF when using the PRI of PS was misleading. In fact, CHDF provided acceptable average particle size values for each mode, but their relative number concentrations were highly erroneous.

Although CHDF has been used extensively to estimate the PSD of colloids, its main drawbacks have not yet been discussed in the literature. In this work, the impact of the main sources of errors when analyzing the PSD of a colloid by CHDF is investigated. First, numerical simulations are implemented to investigate the influences of the diameter calibration, the PRI, and the IB on the estimated PSD. Then, motivated by the highly challenging problem of characterizing the bimodal latexes often required to produce high solids content latexes (Mariz et al., 2010, 2011), a bimodal sample prepared by blending two latexes of MMA/BA/AA is analyzed in commercial CHDF equipment. The raw fractogram is used to estimate the PSD, and the errors in the average particle sizes and the number concentration of each mode are determined by comparison with TEM and DLS measurements.

Analysis of errors in CHDF through numerical examples

Consider two number PSDs, f_1 and f_2, with submicrometric PS particles. The PSDs are discrete, with ordinates given at intervals of $\Delta D = 1$ nm (Fig. 1(a)). The PSD f_1 is unimodal and exhibits an asymmetrical Normal-Logarithmic distribution, given by:

$$f_1(D_i) = \frac{\Delta D}{D_i \sigma_{NL} \sqrt{2\pi}} e^{\left[-[\ln(D_i/\bar{D}_{NL})]^2/2\sigma_{NL}^2\right]}, \tag{8}$$

with geometric average diameter $\bar{D}_{NL} = 85$ nm and standard deviation $\sigma_{NL} = 0.15$. The PSD f_2 is bimodal and was obtained by combining two Normal-Logarithmic distributions, $f_{2,1}$ and $f_{2,2}$, with a relative number concentrations of $c_{n,1} = 85\%$ and $c_{n,2} = 15\%$, respectively, with $\bar{D}_{NL} = 100$ nm and $\sigma_{NL} = 0.1$ for $f_{2,1}$, and $\bar{D}_{NL} = 300$ nm and $\sigma_{NL} = 0.05$ for $f_{2,2}$. The two modes are indicated with (1) and (2) in Fig. 1(a).

The fractograms were simulated through Eqs. (1)–(3a). The nonlinearity of the term $Q_{ext}D_i^2(R_i)$ in the denominator of Eq. (3a) is shown in Fig. 1(b). Assume a "true" calibration $D_i^t(R_i)$ as obtained from Eq. (5) with $K_1 = 1.968$, $K_2 = 0.0029$, and $K_3 = -4.749$ (Fig. 1(c)). The simulated IB-free fractograms $\tau_{R,1}(R_i)$ and $\tau_{R,2}(R_i)$ (Fig. 1(c)) were obtained by substituting f_1, f_2, and $D_i^t(R_i)$ into Eq. (3a). Then, the fractograms $\tau_1(t_i)$ and $\tau_2(t_i)$ of Fig. 1(d) were obtained from $\tau_{R,1}(R_i)$, $\tau_{R,2}(R_i)$, and Eqs. (1) and (2), with a typical marker time $t_m = 960$ s. In contrast to Fig. 1(a), note the following: (i) mode (2) of $\tau_{R,2}(R_i)$ is larger than mode (1), due to the influence of $Q_{ext}D_i^2(R_i)$ in Eq. (3a); and (ii) mode (1) of $\tau_2(t_i)$ appears at higher times, as a consequence of the inverse relationship in Eq. (1). Due to these nonlinear transformations, the fractograms are not proportional to the PSDs, and therefore, the UV detector cannot be considered as an absolute detector of the particle number.
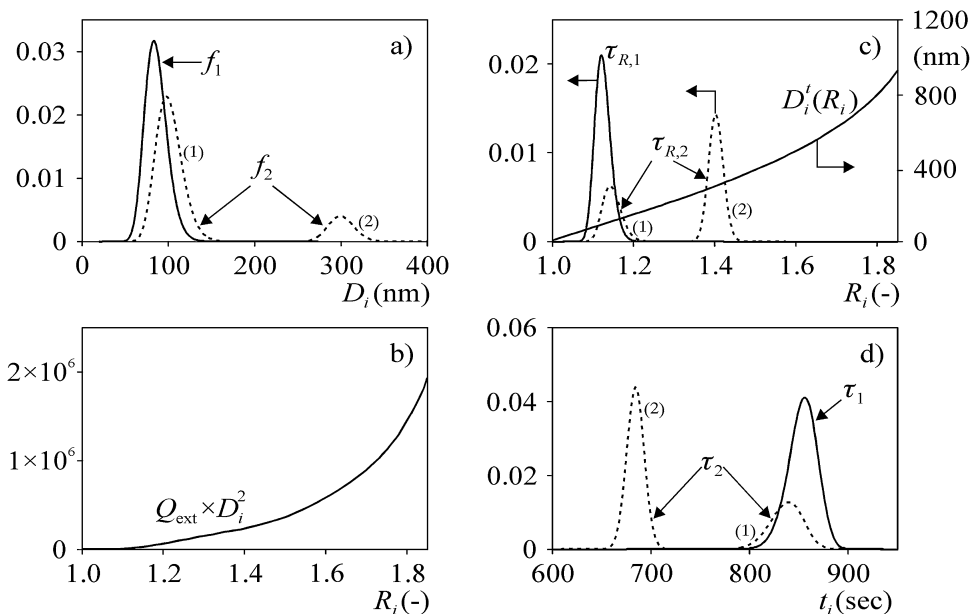
In what follows, the influence of calibration errors, uncertainties in the PRI, and inaccurately corrected IB are studied. To evaluate the quality of an estimated PSD ($\hat{f}$), the following variables are defined (the symbol "^" indicates an estimated value):

$$\bar{D}_{\hat{f}} = \frac{\sum_{i=1}^{N} D_i \hat{f}(D_i)}{\sum_{i=1}^{N} \hat{f}(D_i)}, \tag{9a}$$

$$E_{\hat{f}}(\%) = \left[\frac{\sum_{i=1}^{N} [\hat{f}(D_i) - f(D_i)]^2}{\sum_{i=1}^{N} f(D_i)^2}\right]^{1/2} \times 100, \tag{9b}$$

$$\hat{c}_{n,k}(\%) = \frac{\sum_{i=1}^{N} \hat{f}_{2,k}(D_i)}{\sum_{i=1}^{N} \hat{f}_2(D_i)} \times 100, \quad (k = 1, 2) \tag{9c}$$

where $\bar{D}_{\hat{f}}$ is the number-average diameter of $\hat{f}$, $E_{\hat{f}}(\%)$ is a percentage index error that quantifies the deviation between the estimated and true PSDs, and $\hat{c}_{n,k}$ is the percentage concentration of the mode k ($k = 1, 2$) of f_2.

Fig. 1. Basic simulation data: (a) PSDs, $f_1(D_i)$ and $f_2(D_i)$; (b) term $Q_{ext}D_i^2(R_i)$ in the denominator of Eq. (3a); (c) "true" sigmoidal calibration $D_i^t(R_i)$ and time-relative fractograms, $\tau_{R,1}(R_i)$ and $\tau_{R,2}(R_i)$; and (d) fractograms, $\tau_1(t_i)$ and $\tau_2(t_i)$. The modes associated with the bimodal PSD $f_2(D_i)$ are indicated by (1) and (2).

Sensitivity of the PSD estimate to calibration errors

In practice, the diameter calibration obtained from narrow standards is inaccurate because: (i) standards are polydisperse, (ii) only a limited number of standards is available, (iii) uncertainties in the peak diameters of the standards are unavoidable, and (iv) the fractograms are affected by IB. Therefore, only an approximate diameter calibration $\hat{D}(R_i)$ is obtained, and the PSD estimate will exhibit deviations with respect to the true value.

To simulate a typical calibration procedure, consider the set of $J = 7$ narrow PS standards of Gaussian PSDs, $f_{G,j}(D_i)$ ($j = 1, \ldots, 7$), with peak diameters $\bar{D}_{G,j}$ (nm): {40, 100, 200, 350, 500, 750, 800} and standard deviations $\sigma_{G,j}$ (nm): {7.5, 10, 12.5, 12.5, 12.5, 15, 15} (Fig. 2(a)). The corresponding fractograms $\tau_{G,j}(t_i)$ of Fig. 2(b) were calculated from Eqs. (1)–(3a) on the basis of $D_i^t(R_i)$ (Fig. 1(c)), with $t_m = 960$ s, $\lambda_0 = 220$ nm, $n_m(\lambda_0) = 1.3869$ (for pure water; Bohren & Huffman, 1983), and $n_{p,PS}(\lambda_0) = 2.1051 + 0.21008i$ (Inagaki, Arakawa, Hamm, & Williams, 1977). The fractograms $\tau_{G,6}(t_i)$ and $\tau_{G,7}(t_i)$ are almost superposed as a consequence of the reduced resolution of CHDF at low elution times.

The calibration curve $\hat{D}_i(R_i)$ of Fig. 2(c) was estimated by fitting the pairs {$\bar{D}_{G,j}, R_j$} (indicated by crosses) through a fourth-degree polynomial [Eq. (4)], where R_j was assigned to the peak of the jth fractogram. Uncertainties in the standard diameters were simulated by adding to $\bar{D}_{G,j}$ a zero-mean Gaussian random error of standard deviation of 2.5% (as typically observed in the specification of commercial standards). Differences between $\hat{\hat{D}}_i(R_i)$ and $D_i^t(R_i)$ are close to ±25 nm in the middle fractionation range and reach almost 40 nm at high R_i values.

Consider now the effect of the calibration errors on the estimated PSDs $\hat{\hat{f}}_1$ and $\hat{\hat{f}}_2$ (Fig. 3(a) and (b)), which were obtained by processing $\tau_{R,1}(R_i)$ and $\tau_{R,2}(R_i)$ of Fig. 1(c) with the calibration $\hat{\hat{D}}_i(R_i)$ of Fig. 2(c), through Eq. (3a). Important shifts in the estimated PSDs are observed (Fig. 3). The PSD f_1 as well as each mode of f_2 show meaningful errors in the estimated diameters; however, only small deviations in the estimated number concentration of each mode of f_2 were obtained (Table 1).

Sensitivity of the PSD estimate to uncertainties in the particle refractive index

An important drawback when estimating the ordinates of a PSD by CHDF is that the PRI $n_P(\lambda_0)$ must be known to calculate Q_{ext} in Eq. (3a). To evaluate the influence of only uncertainties in the PRI on the estimated PSDs, consider in what follows the simulated PSDs f_1 and f_2 of Fig. 1(a) with the "true" calibration $D_i^t(R_i)$ of Fig. 1(c). Assume that the particles exhibit a refractive index 15% higher than PS at $\lambda_0 = 220$ nm; i.e., $n_P(\lambda_0) = 1.15n_{p,PS}(\lambda_0) = 2.4209 + 0.2416i$. The corresponding fractograms (not shown here) were simulated by substituting f_1, f_2, and the correct PRI, $n_P(\lambda_0)$, into Eq. (3a). Then, from these fractograms, the estimated PSDs $\hat{f}'_1$ and $\hat{f}'_2$ (Fig. 4) were also obtained with Eq. (3a) using the erroneous PRI of PS, $n_{p,PS}(\lambda_0)$. The main results are summarized in Table 1.
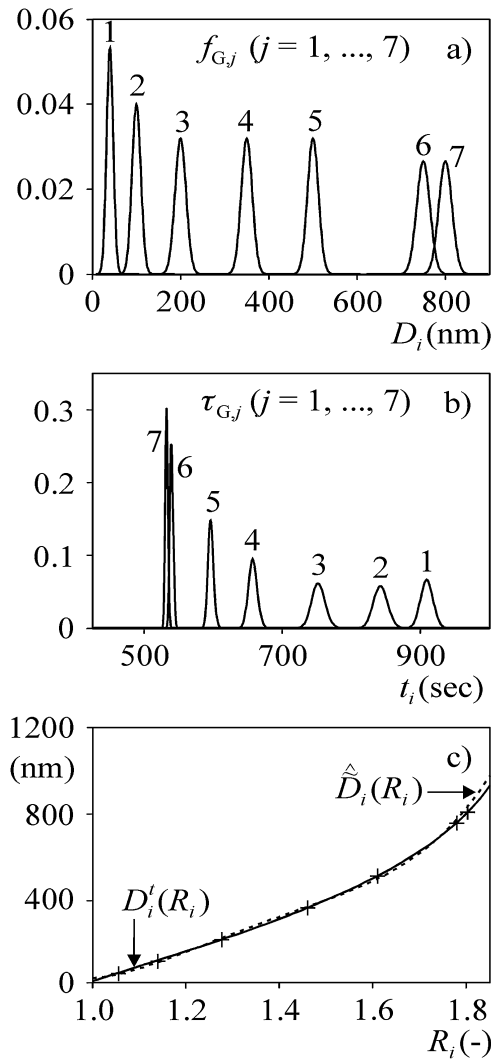
The error of +15% in the PRI produced (Fig. 4 and Table 1) the following: (i) an almost negligible effect on the estimated unimodal PSD f_1; (ii) negligible errors in the average diameters of f_1 and the modes of f_2; and (iii) meaningful errors in the number concentration of the modes of f_2 (note that the estimated mode at large

Table 1

Simulated examples: average diameter ($\bar{D}_f$, in nm) and error index ($E_{\hat{f}}$, in %) for the PSDs estimated by CHDF. For the bimodal PSD f_2, $\hat{c}_{n,k}$ represents the estimated number concentration (in %) of mode k ($k = 1, 2$).

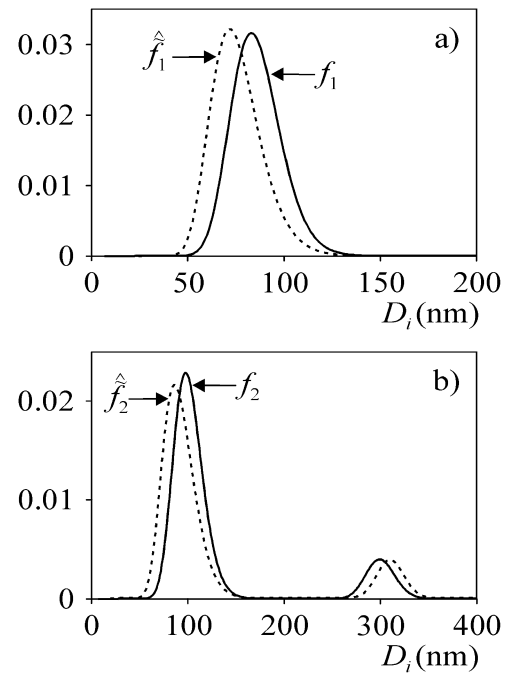| Source of error		f_1	f_2	
			$\hat{f}_{2,1}$	$\hat{f}_{2,2}$
None (true values)	$\bar{D}_f/c_{n,k}$	86.0/–	101/85.0	300/15.0
	$E_{\hat{f}}$	–	–	–
A: Calibration errors	$\bar{D}_{\hat{f}}/\hat{c}_{n,k}$	75.8/–	91.7/86.4	310/13.6
	$E_{\hat{f}}$	59.0	47.6	49.3
B: Uncertainties in PRI	$\bar{D}_{\hat{f}}/\hat{c}_{n,k}$	85.0/–	100/89.7	301/10.3
	$E_{\hat{f}}$	5.15	7.55	31.7
C: Presence of IB	$\bar{D}_{\hat{f}}/\hat{c}_{n,k}$	89.1/–	104/84.2	301/15.8
	$E_{\hat{f}}$	47.0	34.0	98.0
A + B + C	$\bar{D}_{\hat{f}}/\hat{c}_{n,k}$	78.2/–	93.4/92.1	312/7.90
	$E_{\hat{f}}$	74.6	53.8	80.0

Fig. 2. CHDF Calibration with seven PS standards: (a) PSDs of the standards $f_{G,j}(D_i)$ ($j = 1, \ldots, 7$); (b) fractograms of the standards $\tau_{G,j}(t_i)$; and (c) "true" $[(D_i^t(R_i))]$ and estimated $[\hat{\tilde{D}}_i(R_i)]$ calibrations obtained by fitting the pairs $\{\bar{D}_{G,j}, R_j\}$ (indicated by crosses).

Fig. 3. Effect of the calibration error by comparison of the true PSDs (f_1 and f_2) with their estimates ($\hat{\tilde{f}}_1$ and $\hat{\tilde{f}}_2$) on the basis of $\hat{\tilde{D}}_i(R_i)$ of Fig. 2(c).

diameters exhibited a concentration error of approximately 30% with respect to the true value). In addition, in several practical applications, errors greater than 15% in the PRI are possible, and therefore, larger errors in the estimated relative concentrations of multimodal PSDs could be expected.

Sensitivity of the PSD estimate to instrumental broadening

To evaluate the effect of the IB on the estimated PSD, consider a uniform (or time-invariant) IBF $g(t_i, t_{i*})$, modeled through Gaussian distributions of standard deviations equal to 6 s (not shown here). The IB-free fractograms of the simulated calibration standards $\tau_{G,j}(t_i), j = 1, \ldots, 7$ (Fig. 2(b)) were affected by the uniform IBF through Eq. (6), and broadened fractograms $\tau_{G,j}^m(t_i)$ were obtained (Fig. 5(a), solid lines). Fig. 5(b) compares the IB-free (solid lines) and the broadened fractograms (dashed lines). As expected, the narrower fractograms were more affected by IB.
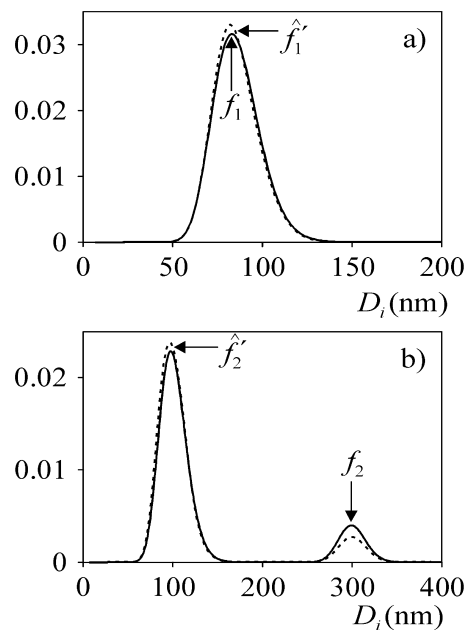
According to the typical approach, the broadened fractograms $\tau_{G,j}^m(t_i)$ were used to estimate the time-variant IBF $\hat{g}(t_i, t_{i*})$, which was assumed to be represented by a set of Gaussian functions of standard deviations $\sigma_g(t_i)$. The values of $\sigma_g(t_i)$ were obtained by
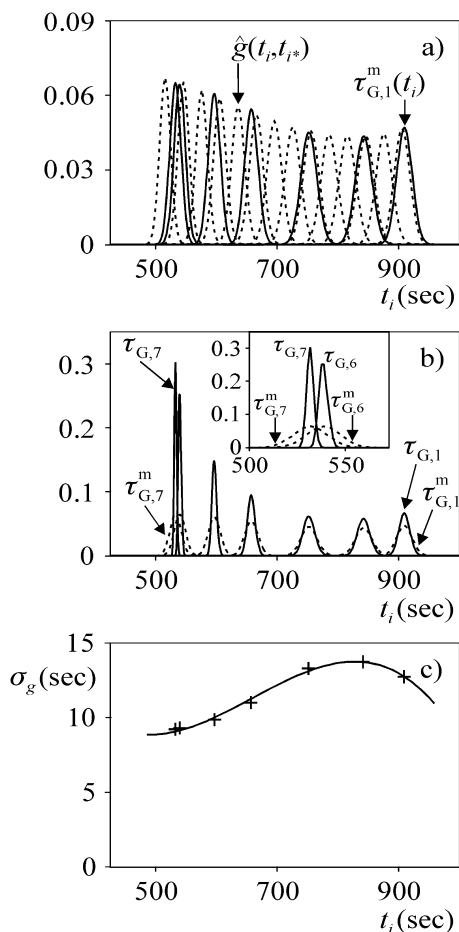
fitting a third-degree polynomial to the standard deviations of $\tau_{G,j}^m(t_i)$, as shown in Fig. 5(c). (The crosses in Fig. 5(c) represent the standard deviations of $\tau_{G,j}^m(t_i)$ placed at the times corresponding to their peak values.) The estimated IBF is represented in dashed lines in Fig. 5(a). As a consequence of the data treatment procedure, the estimated standard deviations $\sigma_g(t_i)$ are greater than the true value (6 s). Fig. 5(a) shows that the measured fractograms are similar to their local IBF estimates.

Considering the simulated PSDs f_1 and f_2 (Fig. 1(a)), their corresponding IB-free fractograms τ_1 and τ_2 (Fig. 1(d)), and the

Fig. 4. Effect of the uncertainties in the PRI by comparison of the true PSDs (f_1 and f_2) with their estimates ($\hat{f}_1'$ and $\hat{f}_2'$) obtained on the basis of an erroneous PRI.

Fig. 5. Effect of IB in CHDF: (a) estimated IBF $\hat{g}(t_i, t_{i*})$, calculated from the fractograms of the standards $\tau_{G,j}^{m}(t_i)$; (b) comparison of IB-free $\tau_{G,j}(t_i)$ and broadened $\tau_{G,j}^{m}(t_i)$ fractograms of the standards; (c) estimated standard deviation of the IBF $\sigma_g(t_i)$, adjusted through a third-degree polynomial: $\sigma_g(t_i) = 70.597 - 0.3133t_i + 5.082 \times 10^{-4}t_i^2 - 2.568 \times 10^{-7}t_i^3$.

time-invariant IBF $g(t_i, t_{i*})$, Fig. 6(a) and (b) compares τ_1 and τ_2 with the broadened fractograms (τ_1^m and τ_2^m) obtained through Eq. (6) and with the IB-corrected fractograms (τ_1^c and τ_2^c) obtained through Eq. (7) with $\hat{g}(t_i, t_{i*})$ of Fig. 5(a) after 50 iterations (a higher number of iterations produced large oscillations in the estimates). The IB-corrected fractograms are narrower than the true ones because $\hat{g}(t_i, t_{i*})$ was broader than $\hat{g}(t_i, t_{i*})$. Fig. 6(c) and (d) shows the corrected PSDs $\hat{f}_1^c$ and $\hat{f}_2^c$ obtained through Eqs. (1)–(3a) from τ_1^c and τ_2^c. As expected, the estimated PSDs are narrower than the true ones.

Due to the overcorrection of the IB and the errors introduced in the numerical inversion (Eq. (7)), the corrected PSDs $\hat{f}_1^c$ and $\hat{f}_2^c$ were distorted and shifted toward larger diameters. Despite such large distortions, the average diameters were only slightly overestimated, and the number concentration of each mode of f_2 was accurately estimated (Table 1).

Combined effects of calibration errors and uncertainties in PRI and IB on the PSD estimate

In practical applications, calibration errors and uncertainties in the PRI and IB simultaneously affect the estimated PSD. Considering the PSDs f_1 and f_2 (Fig. 1(a)) with $n_p(\lambda_0) = 1.15 n_{p,PS}(\lambda_0)$, at $\lambda_0 = 220$ nm, Fig. 7(a) and (b) shows (i) the IB-free fractograms τ_1' and τ_2', obtained through Eqs. (1)–(3a), with $t_m = 960$ s and the true calibration $D_i^t(R_i)$; (ii) the broadened fractograms $\tau_1'^m$ and $\tau_2'^m$,

Table 2
Experimental example: average diameters ($\bar{D}_{\hat{f}}$, in nm) and number concentrations ($\hat{c}_{n,k}$, in %) of each mode of the estimated PSDs with TEM and with CHDF using the PRI of PS, $n_{p,PS}$, and the measured PRI, $\hat{n}_p$ (when assuming a negligible absorption at 220 nm). Average diameters obtained by DLS: 66.0 nm for L_1 and 279 nm for L_2.

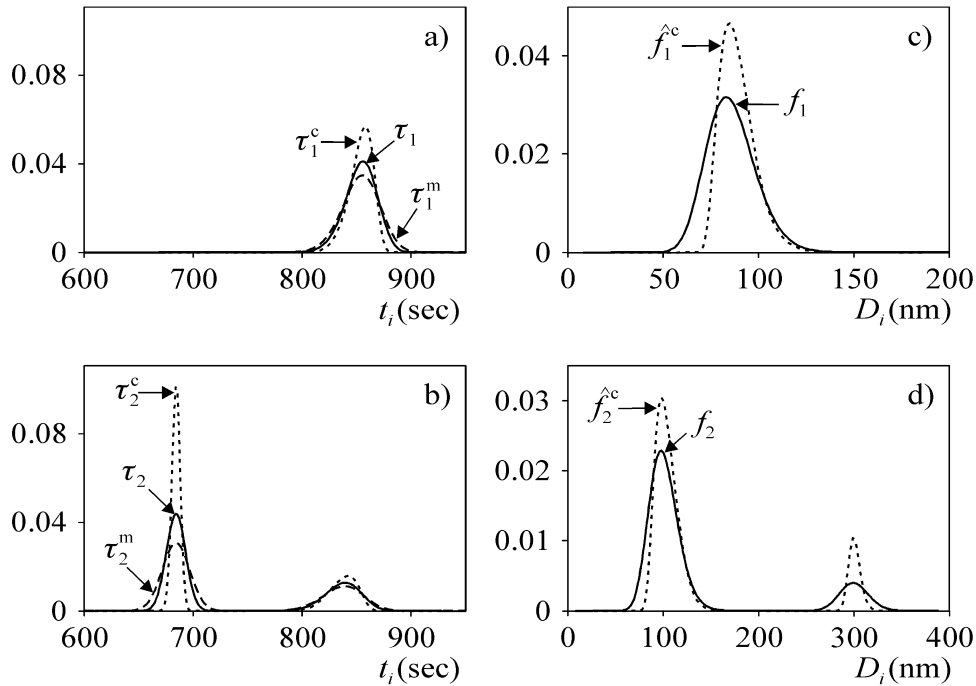|		$\hat{f}_{LX,1}$	$\hat{f}_{LX,2}$
TEM	$\bar{D}_{\hat{f}}$	67.9	290
	$\hat{c}_{n,k}$	98.2	1.8
$n_{p,PS}$	$\bar{D}_{\hat{f}}$	51.4	258
	$\hat{c}_{n,k}$	91.9	8.1
$\hat{n}_p$	$\bar{D}_{\hat{f}}$	49.6	241
	$\hat{c}_{n,k}$	99.1	0.9

obtained through Eq. (6) from τ_1', τ_2', and $g(t_i, t_{i*})$; and (iii) the IB-corrected fractograms $\tau_1'^c$ and $\tau_2'^c$, obtained through Eq. (7) with the estimated IBF, $\hat{g}(t_i, t_{i*})$ (Fig. 5(a)). From $\tau_1'^c$ and $\tau_2'^c$, the estimated IB-corrected PSDs $\hat{\hat{f}}_1'^c$ and $\hat{\hat{f}}_2'^c$ in Fig. 7(c) and (d) were obtained using the erroneous calibration $\hat{D}_i(R_i)$ and the erroneous PRI $n_{p,PS}(\lambda_0)$. Note that the widths of all PSDs were underestimated. Additionally, the number average diameters and the number concentrations of both modes of f_2 were erroneously estimated (Table 1).

Analysis of an experimental sample

This section analyzes the impact the studied sources of errors might have when evaluating the PSD of polymer latexes with unknown PRI in CHDF equipment. To this effect, a copolymer was synthesized by seeded semi-batch emulsion copolymerization with the following monomer weight composition: MMA/BA/AA = 49.5%/49.5%/1%. Two latexes (labeled as L_1 and L_2) with different average particle sizes and unimodal distributions were obtained. Both latexes were blended by adding 40% in weight of L_1 and 60% of L_2 (prepared by gravimetry) to yield a bimodal PSD latex, L_X. Then, the latex L_X was analyzed in a CHDF 2000 (Matec Applied Sciences) instrument and the previously described data treatment was applied to estimate the PSD.

For comparison purposes, the PSDs of modes L_1 and L_2, i.e., f_{L1} and f_{L2} were separately estimated by TEM using an FEI Tecnai G^2 20 Twin electron microscope at 200 kV. Latex samples were adequately diluted and stained with 0.5% aqueous solution of phosphotungstic acid, and a drop of the stained sample was placed on a copper grid covered with formvar (polyvinyl formal, Fluka) and left in the refrigerator at 3 °C. Then, f_{L1} and f_{L2} were estimated by counting more than 500 particles, and the "true" PSD of latex L_X, i.e., f_{LX}, was simply calculated by properly weighting f_{L1} and f_{L2} according to their weight fractions (40% and 60%, respectively). The TEM estimated $\hat{f}_{LX}^{TEM}$ exhibited two modes, $\hat{f}_{LX,1}^{TEM}$ and $\hat{f}_{LX,2}^{TEM}$ (Fig. 8(a)), with percentage number concentrations $c_{n,1} = 98.2\%$ and $c_{n,2} = 1.8\%$, respectively (Table 2). Additionally, the average diameter of modes L_1 and L_2 were estimated with DLS using a Malvern Zetasizer Nano instrument, yielding 66.0 and 279 nm, respectively, which are close to the TEM estimates (Table 2).

Fig. 8(b) presents the fractograms of a set of seven calibration standards (with diameters estimated by DCP: 40, 51, 62, 86, 108, 206, and 348 nm). From the fractograms of Fig. 8(b), the polynomial calibration curve of Fig. 8(c) was obtained by Eq. (4) ($n = 4$). Additionally, the same fractograms were utilized to estimate the IBF, as it was previously described in 'Sensitivity of the PSD estimate to instrumental broadening' section. Finally, Fig. 8(d) compares the measured fractogram τ_{LX}^m with the corrected fractogram τ_{LX}^c calculated with Eq. (7) via 10 iterations (a higher number of iterations produced erroneous spurious modes in τ_{LX}^c). From τ_{LX}^c, the corrected PSD $\hat{f}_{LX}^c$ in Fig. 8(a) was obtained on the basis of Eqs. (1)–(3a), the
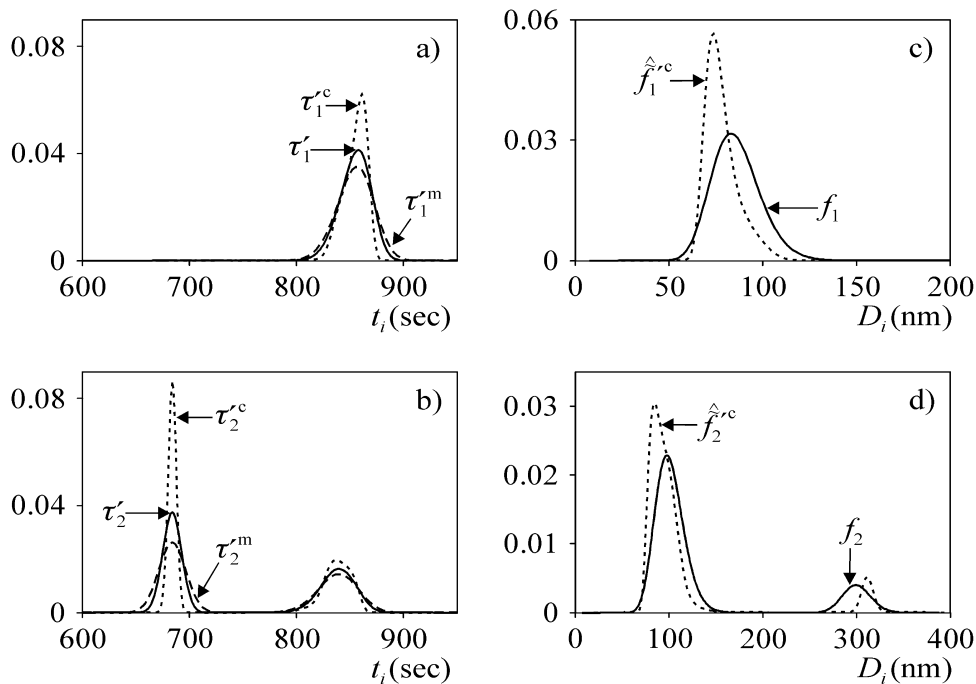
Fig. 6. Effect of the errors in the IB: (a) and (b) IB-free (τ_1, τ_2; solid lines), broadened (τ_1^m, τ_2^m; dashed lines) and corrected (τ_1^c, τ_2^c); dotted lines fractograms corresponding to the true PSDs (f_1, f_2); (c) and (d) true (f_1, f_2; solid lines) and estimated ($\hat{f}_1^c$, $\hat{f}_2^c$; dotted lines) PSDs obtained from the corrected fractograms.

calibration curve of Fig. 8(c), and the erroneous $n_{p,PS}(\lambda_0)$. The average diameter and the number concentration of each mode of $\hat{f}_{LX}^c$ were calculated (Table 2).
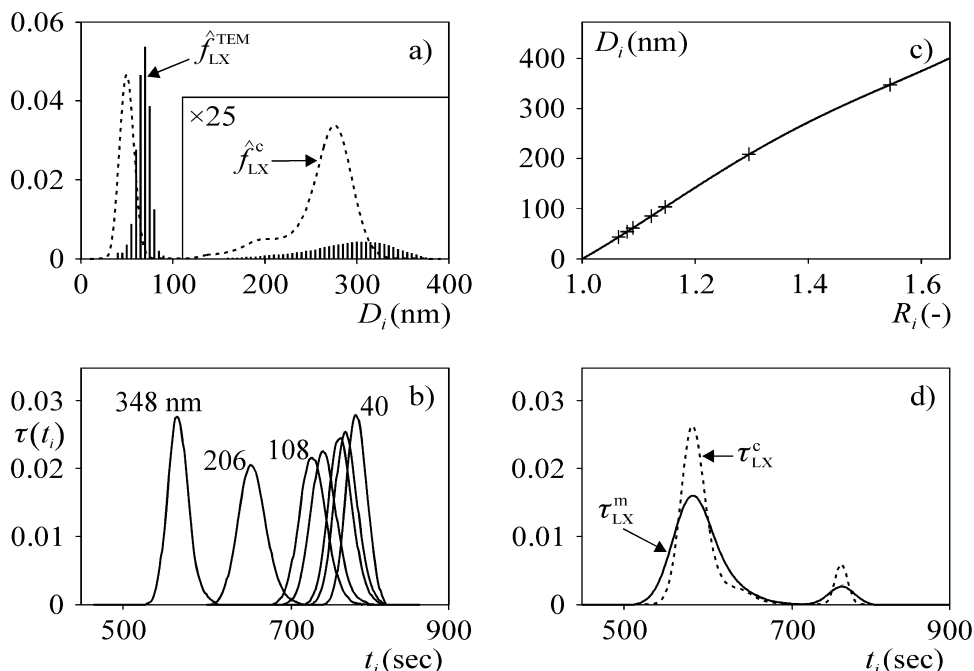
Table 2 and Fig. 8(a) indicate that $\hat{f}_{LX}^c$ exhibits considerable deviations with respect to the TEM estimate. The average diameters of the modes $f_{LX,1}$ and $f_{LX,2}$ deviate around 17 and 31 nm, respectively. These differences can be attributed to an erroneous diameter calibration or an inaccurate IB correction. On the other hand, the

number concentrations of both modes of L_X were also erroneously estimated: $\hat{c}_{n,1} = 91.9\%$ and $\hat{c}_{n,2} = 8.1\%$ (instead of 98.2% and 1.8%, respectively). This result could be due to important differences between the true PRI of the sample and the PRI of PS used for performing the estimation.

To obtain an improved PSD estimation, the PRI was experimentally measured with an attenuated total reflection (ATR) refractometer, following the approach given by Hass, Münzberg,

Fig. 7. Effect of the combined errors: (a) and (b) IB-free (τ_1', τ_2'; solid lines), broadened ($\tau_1'^m$, $\tau_2'^m$; dashed lines), and corrected ($\tau_1'^c$, $\tau_2'^c$; dotted lines) fractograms corresponding to the true PSDs (f_1, f_2), with a PRI 15% larger than PS, at $\lambda_0 = 220$ nm; (c) and (d) true (f_1, f_2; solid lines) and estimated ($\hat{\tilde{f}}_1'^c$, $\hat{\tilde{f}}_2'^c$; dotted lines) PSDs.

Fig. 8. Experimental example: (a) PSDs estimated by TEM ($\hat{f}_{LX}^{TEM}$, vertical bars) and by CHDF ($\hat{f}_{LX}^{c}$, dotted lines) with IB correction; (b) fractograms of the calibration standards (nominal diameters: 40, 51, 62, 86, 108, 206, and 348 nm); (c) estimated diameter calibration; and (d) measured $\tau_{LX}^{m}(t_i)$ and IB-corrected $\tau_{LX}^{c}(t_i)$ fractograms.

Bressel, and Reich (2013), at the wavelengths 469, 705, 778, 840, 906, 935, 960, and 982 nm. The corresponding PRI were 1.48930, 1.47816, 1.47646, 1.47530, 1.47425, 1.47384, 1.47350, and 1.47322 (personal communication with Dr. Oliver Reich, innoFSPEC, Physikalische Chemie, Institut für Chemie, Universität Potsdam, Germany). By assuming a negligible absorption of the acrylic copolymer at the UV region, the PRI at 220 nm was estimated by fitting a second-degree Cauchy polynomial to the measured data, yielding $\hat{n}_p = 1.5628$. Then, the estimated number concentrations of the modes were improved, whereas the corresponding average diameters were slightly deteriorated (see Table 2). The observed deviations with respect to the true values obtained by TEM can be attributed to the hypothesis of non-absorbing particles and also to extrapolation errors caused by the Cauchy polynomial (Gugliotta et al., 2010).

To reinforce the idea on the errors introduced by the calibration procedure, consider that the average diameters of the calibration standards measured by DLS were 43, 56, 63, 93, 115, 211, and 385 nm, which differ from the previously mentioned values obtained by DCP (deviations of up to 10% are observed). Thus, uncertainties in the nominal diameters of the employed standards could have caused large errors in the diameter calibration (as shown in the theoretical analysis of 'Sensitivity of the PSD estimate to calibration errors' section).

Conclusions

PSDs obtained by CHDF are highly sensitive to uncertainties in the diameter calibration, the PRI, and the IB. For instance, small errors in the diameter calibration can produce large deviations in the average diameters and in the shape of the estimated PSDs. Additionally, for bimodal PSDs, calibration errors also affect the estimated number concentrations of the modes.

The estimation of unimodal PSDs is minimally affected by uncertainties in the PRI; therefore, the use of the well-known PRI of PS is acceptable. However, in multimodal PSDs, errors in the PRI can seriously affect the estimated number concentrations of the modes.

Uncorrected IB always leads to PSDs with overestimated widths, and even though it is not shown in this work, this effect is more notorious for narrow PSDs of large diameters. The width of the IBF estimated from the calibration standards was overestimated; therefore, PSDs with underestimated widths were obtained due to the overcorrection of the IB. Additionally, the IB correction procedure can distort the shape of the estimated PSDs.

In practice, calibration errors and uncertainties in the refractive index and IB are simultaneously present, and important deviations in the shape, width, average diameters, and number concentrations (in multimodal distributions) of PSDs are observed. For instance, when using the erroneous PRI of PS in the experimental example, an error greater than 20% was observed in the estimated average diameter of a mode in comparison with the TEM and DLS measurements. Additionally, the estimated number concentration of the mode with smaller fraction was more than four times greater than that obtained from the gravimetric and TEM measurements. This last error diminished when using the experimentally determined PRI.

Even though the results shown in this work were obtained for CHDF, similar analyses can be conducted for fractionation techniques requiring calibration, employing single wavelength turbidity detectors, and exhibiting IB, for example, hydrodynamic chromatography.

Acknowledgements

References

Bohren, C. F., & Huffman, D. R. (1983). *Absorption and scattering of light by small particles*. New York: John Wiley & Sons.

Chu, F., Graillat, C., Guillot, J., & Guyot, A. (1997). Characterization of particle size and size distribution of multi-sized polymer lattices by centrifugation plus quasielastic light scattering. *Colloid and Polymer Science, 275*, 986–991.

DosRamos, J. G., & Silebi, C. A. (1990). The determination of particle size distribution of submicrometer particles by capillary hydrodynamic fractionation (CHDF). *Journal of Colloid and Interface Science, 135*, 165–177.

Elizalde, O., Leal, G. P., & Leiza, J. R. (2000). Particle size distribution measurements: A comparison of four commercial techniques. *Particle and Particle Size Characterization, 17*, 236–243.

Erdem, B., Sully, Y., Sudol, E. D., Dimonie, V. L., & El-Aasser, M. S. (2000). Determination of miniemulsion droplet size via soap titration. *Langmuir, 16*, 4890–4895.

Gugliotta, L. M., Vega, J. R., & Meira, G. R. (1990). Instrumental broadening correction in size exclusion chromatography. Comparison of several deconvolution techniques. *Journal of Liquid Chromatography, 13*, 1671–1708.

Gugliotta, L. M., Clementi, L. A., & Vega, J. R. (2010). Particle size distribution. Main definitions and measurement techniques. In L. M. Gugliotta, & J. R. Vega (Eds.), *Measurement of particle size distribution of polymer latexes* (pp. 1–58). Kerala, India: Research Signpost.

Hass, R., Münzberg, M., Bressel, L., & Reich, O. (2013). Industrial application of photon density wave spectroscopy for in-line particle sizing. *Applied Optics, 52*, 1423–1431.

Inagaki, T., Arakawa, E. T., Hamm, R. N., & Williams, M. W. (1977). Optical properties of polystyrene from the near infrared to the X-ray region and convergence of optical sum rules. *Physical Review B, 15*, 3243–3253.

Ishige, T., Lee, S. I., & Hamielec, H. E. (1971). Solution of Tung's axial dispersion equation by numerical techniques. *Journal of Applied Polymer Science, 15*, 1607–1622.

Jung, K. T., & Shul, Y. G. (2003). Capillary hydrodynamic fractionation studies on the crystal growth of TS-1 zeolite. *Journal of Non-Crystalline Solids, 316*, 246–254.

Lechner, M. D., Colfen, H., Mittal, V., Volkel, A., & Wohlleben, W. (2011). Sedimentation measurements with the analytical ultracentrifuge with absorption optics: Influence of Mie scattering and absorption of the particles. *Colloid and Polymer Science, 289*, 1145–1155.

Mariz, I. D. F. A., De La Cal, J. C., & Leiza, J. R. (2010). Synthesis of high solids content latexes with low viscosities and low particle sizes. *Polymer, 51*, 4044–4052.

Mariz, I. D. F. A., De La Cal, J. C., & Leiza, J. R. (2011). Competitive particle growth: A tool to control the particle size distribution for the synthesis of high solids content low viscosity latexes. *Chemical Engineering Journal, 168*, 938–946.

Mariz, I. D. F. A. (2011). *High solids content low viscosity latexes with small particle size* (Doctoral dissertation). Donostia, Spain: University of the Basque Country UPV/EHU.

Miller, C. M., Venkatesan, J., Silebi, C. A., Sudol, E. D., & El-Aasser, M. S. (1994). Characterization of miniemulsion droplet size and stability using capillary hydrodynamic fractionation. *Journal of Colloid and Interface Science, 162*, 11–18.

Miller, C. M., Sudol, E. D., Silebi, C. A., & El-Aasser, M. S. (1995). Capillary hydrodynamic fractionation (CHDF) as a tool for monitoring the evolution of the particle size distribution during miniemulsion polymerization. *Journal of Colloid and Interface Science, 172*, 249–256.

Silebi, C. A., & DosRamos, J. G. (1989). Separation of submicrometer particles by capillary hydrodynamic fractionation (CHDF). *Journal of Colloid and Interface Science, 130*, 14–24.